A cell-based smoothed finite element method for kinematic limit analysis

Canh V. Le[a], H. Nguyen-Xuan[b], H. Askes[a], S. Bordas[c*], T. Rabczuk[d], H. Nguyen-Vinh[b]

[a] *Department of Civil and Structural Engineering, The University of Sheffield, United Kingdom*
[b] *Department of Mechanics, Faculty of Mathematics and Computer Science, University of Science, VNU-HCM, 227 Nguyen Van Cu, Vietnam*
[c] *Department of Civil Engineering, University of Glasgow, G12 8LT Scotland, UK and Cardiff School of Engineering Theoretical, applied and computational mechanics Cardiff University, UK*
[d] *Institute of Structural Mechanics, Bauhaus-University Weimar, Marienstrae 15, 99423 Weimar*

SUMMARY

This paper presents a new numerical procedure for kinematic limit analysis problems, which incorporates the cell-based smoothed finite element method (CS-FEM) with second-order cone programming. The application of a strain smoothing technique to the standard displacement finite element both rules out volumetric locking and also results in an efficient method that can provide accurate solutions with minimal computational effort. The non-smooth optimization problem is formulated as a problem of minimizing a sum of Euclidean norms, ensuring that the resulting optimization problem can be solved by an efficient second order cone programming algorithm. Plane stress and plane strain problems governed by the von Mises criterion are considered, but extensions to problems with other yield criteria having a similar conic quadratic form or 3D problems can be envisaged.

KEY WORDS: Limit analysis; CS-FEM; strain smoothing; a sum of norms; second order cone programming

1. INTRODUCTION

The computation of the plastic collapse load for limit analysis problems has gained increasing attention in recent years, principally due to the availability of highly efficient optimization algorithms, which have been developing rapidly. Various numerical procedures based on the finite element method have been developed to solve real-world problems in engineering practice [1–5]. Owing to their simplicity, low-order finite elements are often used in these procedures. However, it is well-known that the standard linear displacement finite elements

*Correspondence to: S. Bordas, Department of Civil Engineering, University of Glasgow, G12 8LT Scotland, UK and Cardiff School of Engineering Theoretical, applied and computational mechanics Cardiff University, UK, e-mail: stephane.bordas@alumni.northwestern.edu

exhibit volumetric locking phenomena in the kinematic formulations associated with the von Mises or Tresca yield criteria [4, 6]. In the context of limit analysis, commonly used approaches to overcome this problem are mixed formulations [1,2,7] and kinematic formulations using discontinuity velocity fields [8–10]. Although these methods can provide accurate solutions, their numerical implementation is generally complicated, and have to date not found widespread use in engineering practice. It is therefore desirable to explore alternative methods.

In the effort to further advance meshfree methods, Chen et al. [11] have proposed a strain smoothing technique to stabilize a direct nodal integration in mesh-free methods that use moving least squares (MLS) or reproducing kernel particle (RKP) shape functions. It is known as the stabilized conforming nodal integration (SCNI) scheme. The SCNI scheme has been applied successfully to various problems, for instance, elastic analysis [12–14], plastic limit analysis [15], error estimation [16] and a stabilized mesh-free equilibrium model for limit analysis [17]. It is shown that, when the SCNI scheme is applied, the solutions obtained are accurate and stable, and locking problems can also be prevented. Recently, Liu et al. [18] have applied a strain smoothing technique to a cell/element-based smoothed finite element method (SFEM or CS-FEM) for 2D solids. Subsequently, the theoretical aspects of SFEM were studied in [19, 20], and numerous numerical investigations and applications of SFEM have also been reported [21–26]. It is shown that the method retains most properties of the strain smoothing technique and advantages of FEM, and therefore yields solutions that are accurate, locking free and computational inexpensive. Strain smoothing has then been coupled to the extended finite element method (XFEM) to solve fracture mechanics problems in 2D continuum and plates, e.g. [27]. In addition, the strain smoothing technique has also been applied to the FEM settings to formulate various smoothed finite element methods, including node-based SFEM (NS-FEM) with the upper bound property in strain energy [28], and the edge-based SFEM (ES-FEM) [29,30] and the face-based SFEM (FS-FEM) [31]. Each of these smoothed FEM has different characters and properties, and has been used to produce desired solutions for solid mechanics problems.

Once the displacement/velocity field is approximated and the upper bound theorem is employed, limit analysis becomes an optimization problem. Unfortunately, the objective function in the associated optimization problem is only differentiable in the plastic regions while powerful optimization algorithms require its gradients to be available everywhere. Various techniques have been proposed in the literature to overcome this singularity problem. These include linearization of the yield condition [32], regularization of the plastic dissipation function [33–36], and a direct iterative algorithm [37,38]. One of the most robust and efficient algorithms to overcome this difficulty is the primal-dual interior-point method presented in [39, 40] and implemented in commercial codes such as the Mosek software package. In fact, most commonly used yield criteria can be cast in the form of conic constraints, and optimization problems involving such constraints can be solved using highly efficient primal-dual interior-point solvers [41]. Consequently, several numerical limit analysis procedures which involve the use of cone programming techniques have been reported recently [5, 15, 42–44].

This paper proposes a new numerical procedure for kinematic limit analysis problems, which associates the cell-based smoothed finite element method (CS-FEM) with second-order cone programming to handle accurate solutions for plane stress and plane strain problems. With the use of the strain smoothing scheme in the standard displacement finite element formulations, the volumetric locking problem can be remedied without the need of introducing velocity discontinuities. The non-smooth optimization problem is formulated as a problem of

minimizing a sum of Euclidean norms, ensuring that the resulting optimization problem can be solved by an efficient second order cone programming algorithm. Several numerical examples are given to show the accuracy and effectiveness of the present method.

The layout of the paper is as follows. The next section briefly describes a kinematic upper bound limit analysis formulation for two-dimensional problems. The smoothed finite element method and its properties are presented in Section 3. Discretization of the kinematic formulation using SFEM is described in Section 4. The discretization problem is then formulated as a second-order cone programming in Section 5. Numerical examples are provided in Section 6 to illustrate the performance of the proposed procedure.

2. KINEMATIC LIMIT ANALYSIS

Consider a rigid-perfectly plastic body of area $\Omega \in \mathbb{R}^2$ with boundary Γ, which is subjected to body forces f and to surface tractions g on the free portion Γ_t of Γ. The constrained boundary Γ_u is fixed and $\Gamma_u \cup \Gamma_t = \Gamma$, $\Gamma_u \cap \Gamma_t = \oslash$. Let $\dot{\mathbf{u}} = \begin{bmatrix} \dot{u} & \dot{v} \end{bmatrix}^T$ be plastic velocity or flow fields that belong to a space Y of kinematically admissible velocity fields, where $\dot{u}$ and $\dot{v}$ are the velocity components in x- and y-direction, respectively.

The external work rate associated with a virtual plastic flow $\dot{\mathbf{u}}$ is expressed in the linear form as

$$F(\dot{\mathbf{u}}) = \int_\Omega \mathbf{f}^T \dot{\mathbf{u}} \, \mathrm{d}\Omega + \int_{\Gamma_t} \mathbf{g}^T \dot{\mathbf{u}} \, \mathrm{d}\Gamma \tag{1}$$

If defining $C = \{\dot{\mathbf{u}} \in Y \mid F(\dot{\mathbf{u}}) = 1\}$, the collapse load multiplier λ can be determined by the following mathematical programming

$$\lambda^+ = \min_{\dot{\mathbf{u}} \in C} \int_\Omega D(\dot{\boldsymbol{\epsilon}}) \, \mathrm{d}\Omega \tag{2}$$

where strain rates $\dot{\boldsymbol{\epsilon}}$ are given by

$$\dot{\boldsymbol{\epsilon}} = \begin{bmatrix} \dot{\epsilon}_{xx} \\ \dot{\epsilon}_{yy} \\ \dot{\gamma}_{xy} \end{bmatrix} = \nabla \dot{\mathbf{u}} \tag{3}$$

with ∇_s is the differential operator

$$\nabla = \begin{bmatrix} \dfrac{\partial}{\partial x} & 0 \\ 0 & \dfrac{\partial}{\partial y} \\ \dfrac{\partial}{\partial y} & \dfrac{\partial}{\partial x} \end{bmatrix} \tag{4}$$

The plastic dissipation $D(\dot{\boldsymbol{\epsilon}})$ is defined by

$$D(\dot{\boldsymbol{\epsilon}}) = \max_{\psi(\boldsymbol{\sigma}) \le 0} \boldsymbol{\sigma} : \dot{\boldsymbol{\epsilon}} \equiv \boldsymbol{\sigma}_\epsilon : \dot{\boldsymbol{\epsilon}} \tag{5}$$

in which $\boldsymbol{\sigma}$ represents the admissible stresses contained within the convex yield surface and $\boldsymbol{\sigma}_\epsilon$ represents the stresses on the yield surface associated to any strain rates $\dot{\boldsymbol{\epsilon}}$ through the plasticity condition.

In the framework of a limit analysis problem, only plastic strains are considered and are assumed to obey the normality rule

$$\dot{\boldsymbol{\epsilon}} = \dot{\mu}\frac{\partial \psi}{\partial \boldsymbol{\sigma}} \tag{6}$$

where the plastic multiplier $\dot{\mu}$ is non-negative and the yield function $\psi(\boldsymbol{\sigma})$ is convex. In this study, the von Mises failure criterion is used

$$\psi(\boldsymbol{\sigma}) = \begin{cases} \sqrt{\sigma_{xx}^2 + \sigma_{yy}^2 - \sigma_{xx}\sigma_{yy} + 3\sigma_{xy}^2} - \sigma_0 & \text{plane stress} \\ \sqrt{\frac{1}{4}(\sigma_{xx} - \sigma_{yy})^2 - \sigma_{xy}^2} - \sigma_0 & \text{plane strain} \end{cases} \tag{7}$$

where σ_0 is the yield stress.

Then the power of dissipation can be formulated as a function of strain rates as [1, 15]

$$D(\dot{\boldsymbol{\epsilon}}) = \sigma_0 \sqrt{\dot{\boldsymbol{\epsilon}}^T \boldsymbol{\Theta}\, \dot{\boldsymbol{\epsilon}}} \tag{8}$$

where

$$\boldsymbol{\Theta} = \begin{cases} \dfrac{1}{3}\begin{bmatrix} 4 & 2 & 0 \\ 2 & 4 & 0 \\ 0 & 0 & 1 \end{bmatrix} & \text{plane stress} \\ \\ \begin{bmatrix} 1 & -1 & 0 \\ -1 & 1 & 0 \\ 0 & 0 & 1 \end{bmatrix} & \text{plane strain} \end{cases} \tag{9}$$

Note that condition (6) acts as a kinematic constraint which confines the vectors of admissible strain rates. For plane strain problems, the yield surface $\psi(\boldsymbol{\sigma})$ is unbounded, and the incompressibility condition must be introduced to ensure that the plastic dissipation $D(\dot{\boldsymbol{\epsilon}})$ is finite [2, 7].

3. CELL-BASED SMOOTHED FINITE ELEMENT METHOD (CS-FEM)

The key idea of the cell-based smoothed finite element method (CS-FEM) [18] is to combine the existing finite element method (FEM) with a strain smoothing scheme. In CS-FEM, the problem domain is discretized into elements as in FEM, such as $\Omega = \Omega^1 \cup \Omega^2 \cup \cdots \cup \Omega^{nel}$ and $\Omega^i \cap \Omega_j = \oslash, i \neq j$, and the displacement fields are approximated for each element as

$$\mathbf{u}^h(\mathbf{x}) = \sum_{I=1}^{n} N_I(\mathbf{x})\mathbf{d}_I \tag{10}$$

where n is the number of nodes per element and $\mathbf{d}_I = [\, u_I \;\; v_I \,]^T$ is the nodal displacement vector.

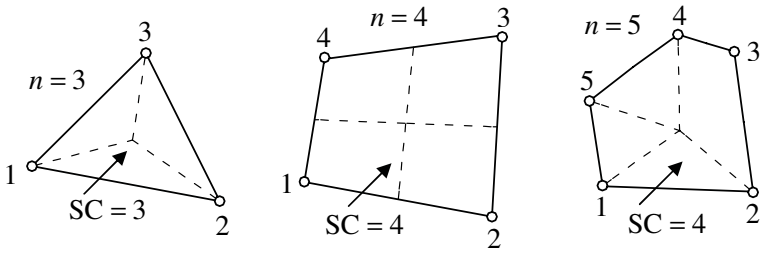

Figure 1. Smoothing cells for various element types: triangular element (left) subdivided into three sub-triangular smoothing cells, quadrilateral element (middle) is partitioned into four subcells and polygonal element (right) subdivided into the shape of triangular and quadrilateral smoothing cells.

Elements are then subdivided into several smoothing cells, such as $\Omega^e = \Omega_1^e \cup \Omega_2^e \cup \cdots \cup \Omega_{nc}^e$, as shown in Figure 1, and smoothing operations are performed for each smoothing cell (SC). A strain smoothing formulation is given by [45]

$$\begin{aligned} \tilde{\boldsymbol{\epsilon}}^h(\mathbf{x}_C) &= \int_{\Omega_C^e} \boldsymbol{\epsilon}^h(\mathbf{x}) \varphi(\mathbf{x}, \mathbf{x} - \mathbf{x}_C)\, \mathrm{d}\Omega \\ &= \int_{\Omega_C^e} \nabla \mathbf{u}^h(\mathbf{x}) \varphi(\mathbf{x}, \mathbf{x} - \mathbf{x}_C)\, \mathrm{d}\Omega \end{aligned} \tag{11}$$

where $\tilde{\boldsymbol{\epsilon}}^h$ is the smoothed value of strains $\boldsymbol{\epsilon}^h$ for smoothing cell Ω_C^e, and φ is a distribution function or a smoothing function that has to satisfy the following properties [45, 46]

$$\varphi \geq 0 \quad \text{and} \quad \int_{\Omega_C^e} \varphi \, \mathrm{d}\Omega = 1 \tag{12}$$

For simplicity, the smoothing function φ is assumed to be a piecewise constant function and is given by

$$\varphi(\mathbf{x}, \mathbf{x} - \mathbf{x}_C) = \begin{cases} 1/A_C, & \mathbf{x} \in \Omega_C^e \\ 0, & \mathbf{x} \notin \Omega_C^e \end{cases} \tag{13}$$

where A_C is the area of the smoothing cell Ω_C^e.

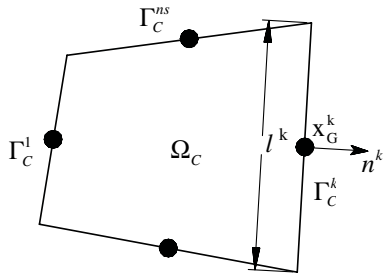

Figure 2. Geometry definition of a smoothing cell

Substituting equation (13) into equation (11), and applying the divergence theorem, one

obtains the following equation

$$\begin{aligned}\tilde{\boldsymbol{\epsilon}}^h(\mathbf{x}_C) &= \frac{1}{A_C}\int_{\Omega_C^e} \nabla \mathbf{u}^h(\mathbf{x})\,\mathrm{d}\Omega \\ &= \frac{1}{A_C}\oint_{\Gamma_C} \mathbf{n}(\mathbf{x})\,\mathbf{u}^h(\mathbf{x})\,\mathrm{d}\Gamma \end{aligned} \tag{14}$$

where Γ_C is the boundary of Ω_C^e and $\mathbf{n}$ is a matrix with components of the outward surface normal given by

$$\mathbf{n} = \begin{bmatrix} n_x & 0 \\ 0 & n_y \\ n_y & n_x \end{bmatrix} \tag{15}$$

Introducing a finite element approximation of the displacement fields, the smooth version of the strain rates can be expressed as

$$\dot{\tilde{\boldsymbol{\epsilon}}}^h(\mathbf{x}_C) = \tilde{\mathbf{B}}\dot{\mathbf{d}} \tag{16}$$

where

$$\dot{\mathbf{d}}^T = [\dot{u}_1, \dot{v}_1, \ldots, \dot{u}_n, \dot{v}_n] \tag{17}$$

$$\tilde{\mathbf{B}} = \begin{bmatrix} \tilde{N}_{1,x}(\mathbf{x}_C) & 0 & \ldots & \tilde{N}_{n,x}(\mathbf{x}_C) & 0 \\ 0 & \tilde{N}_{1,y}(\mathbf{x}_C) & \ldots & 0 & \tilde{N}_{n,y}(\mathbf{x}_C) \\ \tilde{N}_{1,y}(\mathbf{x}_C) & \tilde{N}_{1,x}(\mathbf{x}_C) & \ldots & \tilde{N}_{n,y}(\mathbf{x}_C) & \tilde{N}_{n,x}(\mathbf{x}_C) \end{bmatrix} \tag{18}$$

with

$$\begin{aligned}\tilde{N}_{I,\alpha}(\mathbf{x}_C) &= \frac{1}{A_C}\oint_{\Gamma_C} N_I(\mathbf{x}) n_\alpha(\mathbf{x})\mathrm{d}\Gamma \\ &= \frac{1}{A_C}\sum_{k=1}^{ns} N_I(\mathbf{x}_G^k) n_\alpha^k\, l^k, \quad I = 1, 2, \ldots, n \end{aligned} \tag{19}$$

where $\tilde{N}_{I,\alpha}$ is the smoothed version of shape function derivative $N_{I,\alpha}$; ns is the number of edges of a smoothing cell Ω_C as shown in Figure 2; $\mathbf{x}_G^k$ is the Gauss point (mid-point) of boundary segment Γ_C^k which has length l^k and outward surface normal n^k.

It is evident from Equation (19) that only shape function values at points on the boundaries of the smoothing cells are required in the smoothed strain formulation. This results in the flexibility to compute these shape function values for the CS-FEM, and they can be explicitly obtained using the simple linear point interpolation method without mapping [18]. For four-node quadrilateral elements, values of shape function at integration nodes are given in Figure 3 where these values are indicated in the format (N_1, N_2, N_3, N_4).

With the use of the smoothed strains, the problem integrals can be determined directly by

$$\int_{\Omega^e} \mathscr{F}(\dot{\tilde{\boldsymbol{\epsilon}}}^h)\,\mathrm{d}\Omega = \sum_{C=1}^{nc}\int_{\Omega_C^e} \mathscr{F}(\dot{\tilde{\boldsymbol{\epsilon}}}_C^e)\,\mathrm{d}\Omega = \sum_{C=1}^{nc} A_C \mathscr{F}(\dot{\tilde{\boldsymbol{\epsilon}}}_C^e) \tag{20}$$

where nc is the number of SCs. From Equation (20), it turns out that there is no need of an isoparametric mapping in CS-FEM formulation, and therefore elements with a severely distorted shape can be employed.

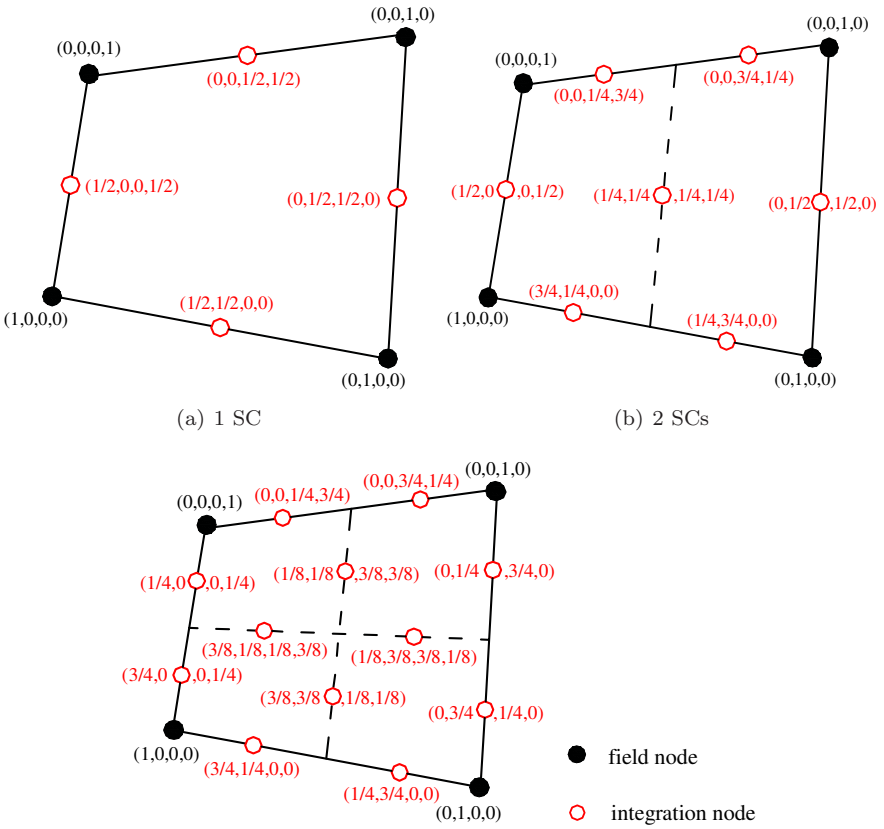

Figure 3. Division of an element into smoothing cells (nc) and the value of the shape function along the boundaries of smoothing cells: (a) the quadrilateral element is considered as one subcell, (b) the element is subdivided into two subcells and (c) the element is partitioned into four subcells.

Theoretical and numerical investigations on the influence of the number of SCs have been carried out in [19,20]. It has been shown that the CS-FEM solution has different properties for different numbers of SCs. Solutions of CS-FEM using a single smoothing cell are equivalent to those obtained by the standard FEM using reduced integration or from a quasi-equilibrium element [20, 27]. This equivalence was explained to be the reason for the superconvergent behavior of the one subcell CS-FEM in elasto-statics. Moreover, the one subcell version is insensitive to volumetric locking in incompressible linear elasticity and elasto-plastic problems. In this paper, we will show that these properties are retained for plastic limit analysis.

4. CS-FEM DISCRETIZATION OF KINEMATIC FORMULATION

In the FEM, the plastic dissipation over the rigid-perfectly plastic body is computed by

$$D^{FEM} = \int_\Omega \sigma_0 \sqrt{\dot{\boldsymbol{\epsilon}}^T \boldsymbol{\Theta}\, \dot{\boldsymbol{\epsilon}}}\, \mathrm{d}\Omega = \sum_{e=1}^{nel} \int_{\Omega^e} \sigma_0 \sqrt{\dot{\boldsymbol{\epsilon}}^{eT} \boldsymbol{\Theta}\, \dot{\boldsymbol{\epsilon}}^e}\, \mathrm{d}\Omega \tag{21}$$

Conversely, in the CS-FEM formulation, the plastic dissipation is expressed as

$$D^{SFEM} = \sum_{e=1}^{nel} \sum_{C=1}^{nc} \int_{\Omega_C^e} \sigma_0 \sqrt{\dot{\tilde{\boldsymbol{\epsilon}}}_C^{eT} \boldsymbol{\Theta}\, \dot{\tilde{\boldsymbol{\epsilon}}}_C^e}\, \mathrm{d}\Omega \tag{22}$$

in which $\dot{\tilde{\boldsymbol{\epsilon}}}_C^e$ is determined by Equation (16).

In the following, we will show that when triangular elements are used (linear shape functions), CS-FEM and FEM are equivalent, $D^{SFEM} \equiv D^{FEM}$, regardless the number of SCs. This proof is a straightforward extension of the argument presented in [19]. When linear shape functions are used, the strain rates $\dot{\boldsymbol{\epsilon}}^e$ are constant over whole element Ω^e. Consequently, one obtains the following estimation

$$\dot{\tilde{\boldsymbol{\epsilon}}}_C^e = \int_{\Omega_C^e} \frac{\dot{\boldsymbol{\epsilon}}^e}{A_C}\, \mathrm{d}\Omega = \dot{\boldsymbol{\epsilon}}^e \int_{\Omega_C^e} \frac{1}{A_C}\, \mathrm{d}\Omega = \dot{\boldsymbol{\epsilon}}^e \tag{23}$$

which implies that the smoothed strain rates over the smoothing cell Ω_C^e are identical to those over the element Ω^e.

With the use of the relation (23), the plastic dissipation becomes

$$\begin{aligned} D^{SFEM} &= \sum_{e=1}^{nel} \sum_{C=1}^{nc} \int_{\Omega_C^e} \sigma_0 \sqrt{\dot{\boldsymbol{\epsilon}}_C^{eT} \boldsymbol{\Theta}\, \dot{\boldsymbol{\epsilon}}_C^e}\, \mathrm{d}\Omega \\ &= \sum_{e=1}^{nel} \sigma_0 \sqrt{\dot{\boldsymbol{\epsilon}}_C^{eT} \boldsymbol{\Theta}\, \dot{\boldsymbol{\epsilon}}_C^e} \sum_{C=1}^{nc} \int_{\Omega_C^e} \mathrm{d}\Omega = \sum_{e=1}^{nel} \sigma_0 \sqrt{\dot{\boldsymbol{\epsilon}}^{eT} \boldsymbol{\Theta}\, \dot{\boldsymbol{\epsilon}}^e} \int_{\Omega^e} \mathrm{d}\Omega \\ &= \sum_{e=1}^{nel} \int_{\Omega^e} \sigma_0 \sqrt{\dot{\boldsymbol{\epsilon}}^{eT} \boldsymbol{\Theta}\, \dot{\boldsymbol{\epsilon}}^e}\, \mathrm{d}\Omega = D^{FEM} \end{aligned} \tag{24}$$

In the case when bilinear quadrilateral elements are used, the strain rates are a linear function of coordinates, which means $\dot{\boldsymbol{\epsilon}}^e \neq \dot{\tilde{\boldsymbol{\epsilon}}}_C^e$ and $D^{FEM} \neq D^{SFEM}$. Hence, the solution obtained using CS-FEM is different from that obtained using the standard FEM. With this in mind, to make reasonable comparison with the standard FEM, the bilinear quadrilateral CS-FEM will be used in the solution procedure described in the following section. Note that the smoothed strain rates $\dot{\tilde{\boldsymbol{\epsilon}}}_C^e$ are constant over smoothing cell Ω_C^e, and Equation (22) can be rewritten as

$$D^{SFEM} = \sum_{e=1}^{nel} \sum_{C=1}^{nc} \sigma_0 A_C \sqrt{\dot{\tilde{\boldsymbol{\epsilon}}}_C^{eT} \boldsymbol{\Theta}\, \dot{\tilde{\boldsymbol{\epsilon}}}_C^e} \tag{25}$$

Hence the optimization problem (2) can now be rewritten as

$$\begin{aligned} \lambda^+ &= \min \sum_{e=1}^{nel} \sum_{C=1}^{nc} \sigma_0 A_C \sqrt{\dot{\boldsymbol{\epsilon}}_C^{eT} \boldsymbol{\Theta} \dot{\boldsymbol{\epsilon}}_C^e} \\ &\text{s.t} \begin{cases} \dot{\mathbf{u}} = \mathbf{0} & \text{on } \Gamma_u \\ F(\dot{\mathbf{u}}) = 1 \end{cases} \end{aligned} \tag{26}$$

It is important to note that the enforcement of boundary conditions in CS-FEM and FEM formulations is identical. For plane strain problems the incompressibility constraint is also enforced in problem (26). The assumed strains using strain smoothing defined in Equation (11) relax the compatibility somewhat. It is therefore no longer possible to guarantee that the solution obtained from the problem (26) is a strict upper bound on the collapse multiplier of the original, continuous problem. However, using the smoothed strain rates which are constant over a smoothing cell, the flow rule (or incompressibility condition in plane strain) only needs to be enforced at any one point in each smoothing cell, and it is guaranteed to be satisfied everywhere in the problem domain. Therefore, the computed collapse load obtained using the proposed method still can reasonably be considered as an upper bound on the actual value.

5. SOLUTION OF THE DISCRETE PROBLEM

The limit analysis problem (26) is a non-linear optimization problem with equality constraints. In fact, the problem can be reduced to the problem of minimizing a sum of norms, as described below.

Since $\boldsymbol{\Theta}$ is a positive definite matrix in plane stress problems (see in Equation (9)), the objective or the plastic dissipation function in (26) can be rewritten straightforwardly in a form involving a sum of norms as

$$D^{SFEM} = \sum_{e=1}^{nel} \sum_{C=1}^{nc} \sigma_0 A_C \left|\left| \mathbf{C}^T \dot{\boldsymbol{\epsilon}}_C^e \right|\right| \tag{27}$$

where $||.||$ denotes the Euclidean norm appearing in the plastic dissipation function, i.e, $||\mathbf{v}|| = (\mathbf{v}^T\mathbf{v})^{1/2}$, $\mathbf{C}$ is the so-called Cholesky factor of $\boldsymbol{\Theta}$

$$\mathbf{C} = \frac{1}{\sqrt{3}} \begin{bmatrix} 2 & 0 & 0 \\ 1 & \sqrt{3} & 0 \\ 0 & 0 & 1 \end{bmatrix} \tag{28}$$

For convenience, a vector of additional variables $\boldsymbol{\rho}_1$ is introduced as

$$\boldsymbol{\rho}_1 = \begin{bmatrix} \rho_1 \\ \rho_2 \\ \rho_3 \end{bmatrix} = \mathbf{C}^T \dot{\boldsymbol{\epsilon}}_C^e \tag{29}$$

Hence, Equation (31) becomes

$$D^{SFEM} = \sum_{e=1}^{nel} \sum_{C=1}^{nc} \sigma_0 A_C \left|\left| \boldsymbol{\rho}_1 \right|\right| \tag{30}$$

For plane strain problems, the determinant of the matrix $\mathbf{\Theta}$ is equal to zero and its Cholesky factor does not exist. Therefore, the above technique cannot be applied to this case. However, it is still possible to transform problem (26) to a problem of minimizing a sum of norms, as follows.

First, the objective function in the above optimization problem is rewritten as

$$D^{SFEM} = \sum_{e=1}^{nel} \sum_{C=1}^{nc} \sigma_0 A_C \sqrt{(\dot{\tilde{\epsilon}}^e_{xxC} - \dot{\tilde{\epsilon}}^e_{yyC})^2 + (\dot{\tilde{\gamma}}^e_{xyC})^2} \tag{31}$$

Similarly, a vector of additional variables $\boldsymbol{\rho}_2$ is introduced as

$$\boldsymbol{\rho}_2 = \begin{bmatrix} \rho_1 \\ \rho_2 \end{bmatrix} = \begin{bmatrix} (\dot{\tilde{\epsilon}}^e_{xxC} - \dot{\tilde{\epsilon}}^e_{yyC}) \\ \dot{\tilde{\gamma}}^e_{xyC} \end{bmatrix} \tag{32}$$

The plastic dissipation is then expressed as

$$D^{SFEM} = \sum_{e=1}^{nel} \sum_{C=1}^{nc} \sigma_0 A_C \, ||\boldsymbol{\rho}_2|| \tag{33}$$

Now the optimization problem (26) becomes a problem of minimizing a sum of norms as

$$\begin{aligned} \lambda^+ \quad = \quad & \min \sum_{e=1}^{nel} \sum_{C=1}^{nc} \sigma_0 A_C \, ||\boldsymbol{\rho}_\alpha|| \\ & \text{s.t} \begin{cases} \dot{\mathbf{u}} = \mathbf{0} & \text{on } \Gamma_u \\ F(\dot{\mathbf{u}}) = 1 \end{cases} \end{aligned} \tag{34}$$

where $\alpha = 1$ for plane stress and $\alpha = 2$ for plane strain. In fact a problem of this sort can be cast as a second-order cone programming (SOCP) problem by introducing auxiliary variables $t_1,\ t_2,\ \ldots,\ t_{nel \times nc}$

$$\begin{aligned} \lambda^+ \quad = \quad & \min \sum_{j=1}^{nel \times nc} \sigma_0 A_j t_j \\ & \text{s.t} \begin{cases} \dot{\mathbf{u}} = \mathbf{0} & \text{on } \Gamma_u \\ F(\dot{\mathbf{u}}) = 1 \\ ||\boldsymbol{\rho}_\alpha||_i \leq t_i \quad i = 1, 2, \ldots, nel \times nc \end{cases} \end{aligned} \tag{35}$$

where the third constraint in problem (35) represents quadratic cones, and $\boldsymbol{\rho}_\alpha$ is defined by Equations (29) and (32).

6. NUMERICAL EXAMPLES

This section will investigate the performance of the proposed solution procedure via a number of benchmark problems in which analytical and other numerical solutions are available. All examples are considered in either plane stress or plane strain state and the von Mises criterion is exploited. Our objective is to draw conclusions particularly on the accuracy of solutions,

convergence rate, incompressibility locking under plane strain conditions and the efficiency of the presented method in large-scale computation. The following models are used for comparison purpose:

- FEMQ4– standard bilinear four-noded quadrilateral element using full integration (2×2 Gauss points)
- FEMRI– standard bilinear four-noded quadrilateral element using reduced integration (1 Gauss point)
- CS-FEMk– SFEM four-noded quadrilateral element with k smoothing cells or subcells, whereby $k = 1, 2$ and 4

6.1. Square plate with a central circular hole

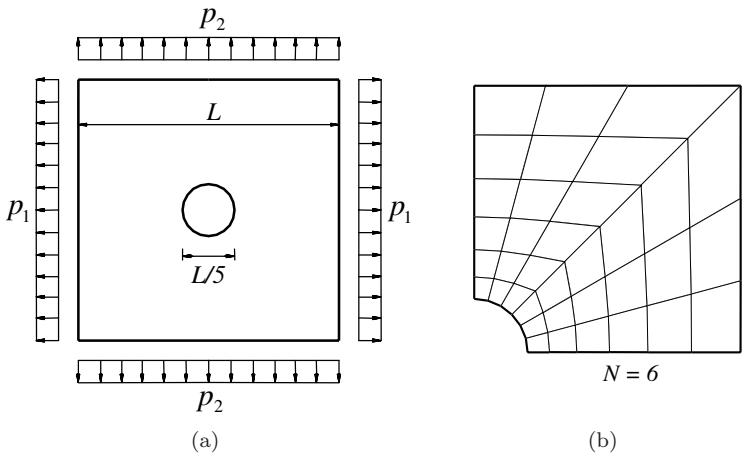

Figure 4. A square plate with a circular hole: (a) geometry and loading, (b) finite element mesh

The first example deals with a square plate with a central circular hole which is subjected to biaxial uniform loads p_1 and p_2 as shown in Figure 4a, where $L = 10$ m. This benchmark plane stress problem has been solved numerically for different loading cases by finite element models [4, 6, 47–49], by the boundary element method (BEM) [50] and more recently by the element-free Galerkin (EFG) method [51]. Due to symmetry, only the upper-right quarter of the plate is modeled, see Figure 4b. Symmetry conditions are enforced on the left and bottom edges.

The procedure was first applied to the plate with $p_2 = 0$ for which analytical solutions are available [52], namely $\lambda = 0.8\frac{p_1}{\sigma_0}$, thereby enabling objective validation. Numerical solutions obtained for different models with variation of N are shown in Table I. From these results, it can be observed that in all cases CS-FEM always provides more accurate solutions than FEMQ4, and that the collapse load multiplier of CS-FEM will approach the FEM solution as the number of smoothing cells increases. Furthermore, although it has been pointed out that the proposed procedure cannot be guaranteed to provide strict upper bound solutions, it is clear that all the solutions obtained are above the exact value. For all mesh cases, the solution obtained by CS-FEM with $nc = 1$ is smallest and most accurate.

Table I. Collapse load multiplier of the plate with variation of N ($p_2 = 0$)

Models	$N \times N$				Analytical solution
	6×6	12×12	24×24	48×48	
CS-FEM1	0.8151	0.8047	0.8017	0.8006	0.800
CS-FEM2	0.8216	0.8078	0.8035	0.8018	
CS-FEM4	0.8226	0.8085	0.8038	0.8019	
FEMQ4	0.8238	0.8090	0.8041	0.8021	

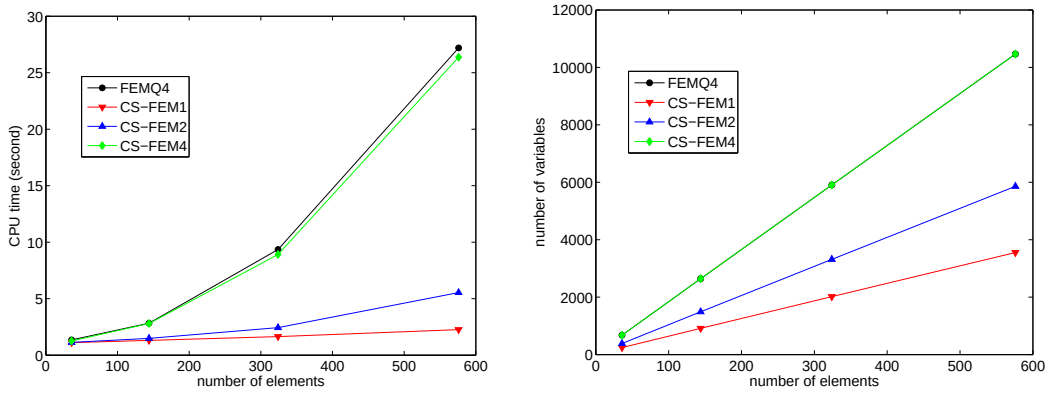

(a) Computational cost

(b) Variables in the optimization problem

Figure 5. Comparison of CPU time and variables between FEM and CS-FEM for different meshes with $p_2 = 0$ (the code is written using MATLAB and was run using a 2.8 GHz Pentium 4 PC running Microsoft XP)

Figure 5 illustrates the computing time and the number of variables in the optimization problem against the number of elements. Note that CPU time reported here was taken to calculate shape function derivatives (smoothed value for CS-FEM), and to build and solve the optimization problem. It can be seen from the Figure that both FEMQ4 and CS-FEM4 give rise to problems with an identical number of variables for each mesh. However, less CPU time is required when using the CS-FEM4 model. The difference comes from the fact that the FEMQ4 element needs to determine the Jacobian determinant, the inverse of the Jacobian matrix while the CS-FEM4 element does not. The difference in CPU time is even more marked when either CS-FEM2 or CS-FEM1 are used. This is because the number of variables in the underlying optimization problem of CS-FEM2 and CS-FEM1 is much smaller than when using FEMQ4.

The convergence rate is also illustrated by Figure 6. It is evident that all numerical solutions converge to the exact solution as the mesh size h tends to zero. For cases when $nc = 2$ or $nc = 4$, convergence rate of CS-FEM is slightly higher than that of FEM. The most remarkable result is observed in the extreme case when $nc = 1$, which yields superconvergent behaviour. It is seen that the convergence rate of CS-FEM also tends to that of FEM when increasing the number of SCs. In summary, CS-FEM with the single smoothing cell appears to offer a good combination of accuracy and computational efficiency for plastic limit analysis problems. With

this in mind, the one subcell version of CS-FEM will be used for other loading cases considered hereafter for this problem. In linear statics, the one subcell version is known to be unstable, but, as seen and discussed below, this problem does not plague the optimization process used in limit analysis.

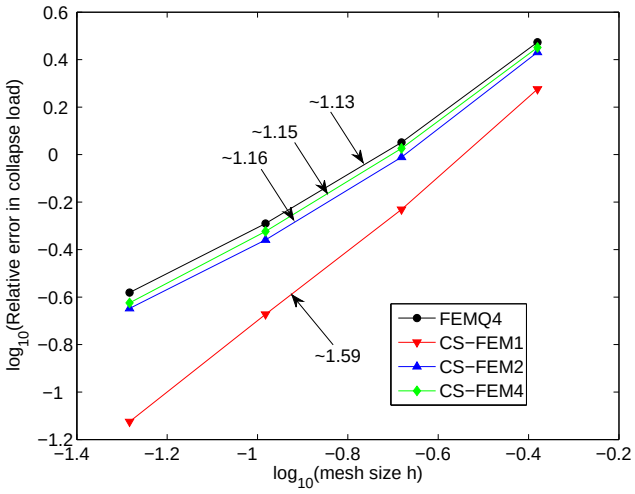

Figure 6. Convergence rate with $p_2 = 0$ (values indicated in the figure are approximated slopes)

Table II compares solutions obtained using the present method with solutions obtained previously by different limit analysis approaches (kinematic or static) using FEM or BEM or EFG simulations. Note that in [6] displacement elements with p-version were used within a static approach and therefore the method does not guarantee a lower bound collapse limit. In other words, the static method in [6] may provide a higher solution than the actual collapse multiplier, such as for the $p_2 = 0$ loading case. A similar phenomenon can be observed in [50] where the static conditions were not strictly satisfied. The estimated lower-bound in [50] surpasses the upper-bound of the present method and [4] when $p_2 = p_1$ or $p_2 = p_1/2$. In general, the present solutions are in good agreement with results in the literature. Furthermore, the present solution procedure with the use of second-order cone programming (SOCP) is efficient and robust since just less than 5 seconds[†] were taken to solve the optimization problem here, with 14018 variables and 7011 constraints.

Considering previously obtained upper-bound solutions, the present method provides lower (more accurate) solutions than in [4] for all loading cases, despite the fact that the number of elements used in the present method is significantly smaller than in [4]. Figure 7 illustrates the patterns of plastic energy dissipation and collapse mechanisms for different loading cases are also shown in Figure 8, where the deformation is calculated by multiplying the computed collapse velocity by a suitable time scale and then adding it to the original grid. It can be seen

[†]the code is written using MATLAB and was run using a 2.8 GHz Pentium 4 PC running Microsoft XP

from Figure 7 that the plastic dissipation is clearly concentrated on plastic zones in the form of slip lines, which is somewhat different from the more dilute failure zones shown in [4].

Table II. Collapse load multiplier with different loading cases and $N = 48$ compared with previously obtained solutions

Approach	Authors	Loading cases		
		$p_2 = p_1$	$p_2 = p_1/2$	$p_2 = 0$
Kinematic (upper bound)	Vicente da Silva and Antao [4]	0.899	0.915	0.807
	Present method	0.895	0.911	0.801
Mixed formulation	Zouain et al. [53]	0.894	0.911	0.803
Analytical solution [52]		–	–	0.800
Static (lower bound)	Tin-Loi and Ngo [6]	0.895‡	0.912‡	0.803‡
	Liu et.al. [50]	0.903‡	0.915‡	0.795‡
	Chen et.al. [51]	0.874	0.899	0.798
	Gross-Weege [49]	0.882	0.891	0.782
	Belytschko [47]	–	–	0.780
	Nguyen-Dang and Palgen [48]	0.704	–	0.564

‡ where a true lower bound on collapse limit is not guaranteed

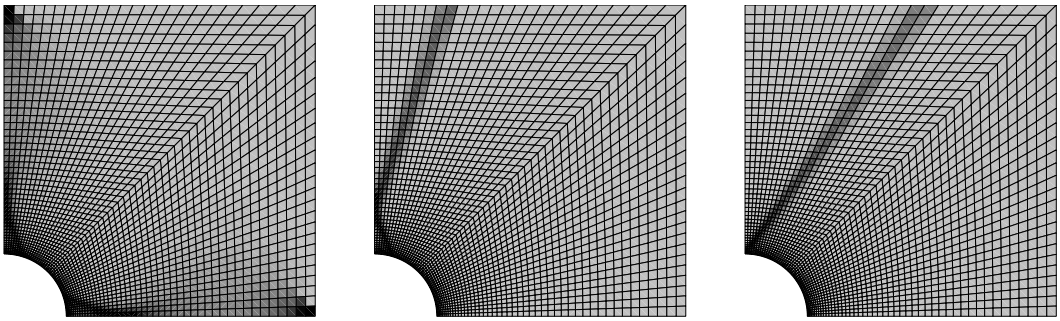

(a) (b) (c)

Figure 7. Plastic dissipation distribution for different loading cases: (a) $p_2 = p_1$, (b) $p_2 = p_1/2$ and (c) $p_2 = 0$

6.2. Double notched tensile specimen

This problem was introduced to illustrate locking phenomena by Nagtegaal et al. [54] and became a popular benchmark test for plastic analysis procedures, particularly for rigid-plastic limit analysis [2, 3, 5, 55, 56]. The test problem consists of a rectangular specimen with two external thin symmetric cuts under in-plane tensile stresses τ_0, as shown in Figure 9. Taking advantage of symmetry, only the upper-right quarter of the specimen was discretized (Figure 9)

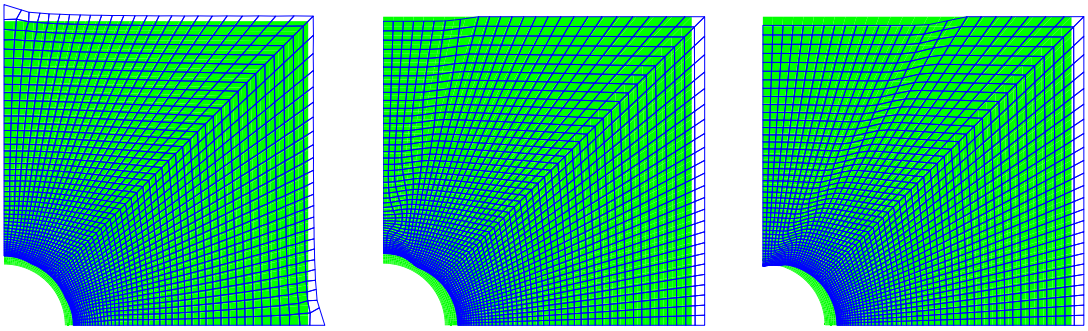

(a) (b) (c)

Figure 8. Collapse mechanisms (original shape in green) with different loading cases: (a) $p_2 = p_1$, (b) $p_2 = p_1/2$ and (c) $p_2 = 0$

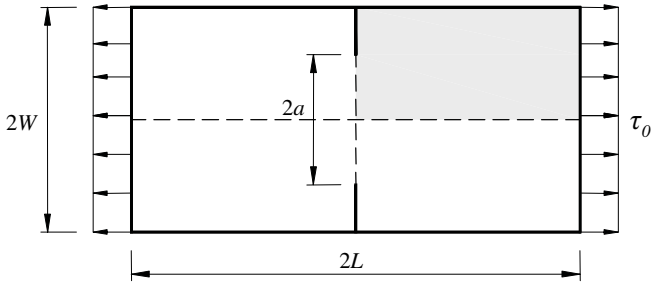

Figure 9. The test problem in plane strain: geometry ($W = L = 1$) and loading

and appropriate boundary conditions were applied.

First, volumetric locking behavior and the effect of mesh distortion on the solutions are studied. Both regular and irregular elements are considered (Figure 10). Coordinates of interior nodes are controlled by [18]

$$\begin{aligned} x' &= x + r \cdot \alpha_{ir} \cdot \Delta x \\ y' &= y + r \cdot \alpha_{ir} \cdot \Delta y \end{aligned} \tag{36}$$

where $r \in [-1,\ 1]$ is a computer-generated random number, the α_{ir} parameter is used to shape the distorted elements and Δx, Δy are initial regular element sizes in the $x-$ and $y-$direction, respectively.

While CS-FEM2 and CS-FEM4 exhibit the same locking problem as the standard FEM with full integration FEMQ4, CS-FEM1 can remedy locking similarly to the FEM with reduced integration (FEMRI). Table III presents the collapse multipliers obtained using CS-FEM1 and FEMRI with different regular meshes. It can be observed that the solutions obtained by CS-FEM1 and FEMRI with regular elements are identical.

To evaluate effect of the shape of the quadrilateral elements on accuracy, a series of analyses using severely distorted elements is performed. The level of nodal irregularity is governed by the distortion parameter α_{ir}. Collapse multipliers obtained using the present procedure with different levels of mesh distortion are shown in Table IV. It is evident that when severely

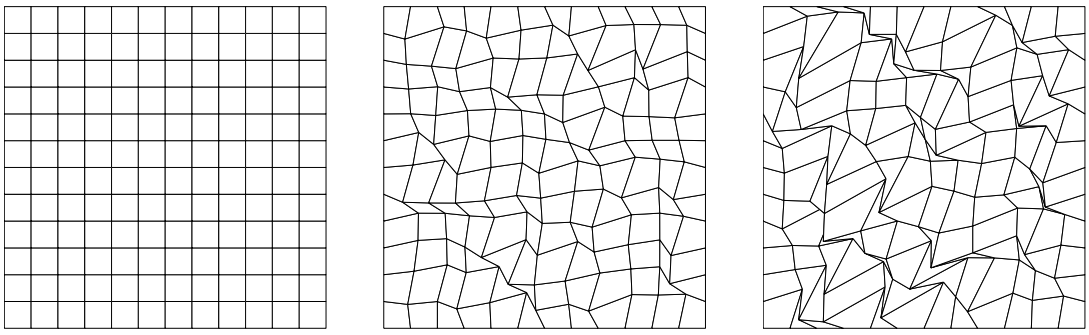

(a) (b) (c)

Figure 10. Meshes: (a) regular, $\alpha_{ir} = 0$; (b) $\alpha_{ir} = 0.4$ and (c) extremely distorted, $\alpha_{ir} = 0.8$

Table III. Collapse multiplier: regular meshes ($a = 1/2$)

Models	$N \times N$			
	6×6	12×12	24×24	48×48
CS-FEM1	1.2684	1.2035	1.1685	1.1504
FEMRI	1.2684	1.2035	1.1685	1.1504

distorted elements ($\alpha_{ir} \geq 0.6$) are used, FEM fails to compute the collapse load limit due to the negative determinant of the Jacobian matrix, whereas CS-FEM1 still works well for all cases. Moreover, the smoothed strain rates in CS-FEM1 elements are constant and hence the flow rule (or incompressibility condition) is satisfied everywhere in the domain. While the strain rates in a standard quadrilateral element are linear, a single integration point cannot guarantee this condition (for this case, at least 4 integration points (on vertices) are needed to ensure the incompressibility condition is satisfied everywhere in the element). It has been reported that in elasto-static and dynamic problems, the CS-FEM1 model may result in unstable solutions due to hourglass modes (zero energy modes) [18, 22]. However, it is evidently seen from our numerical results that the CS-FEM1 model can provide stable solutions for limit analysis problems, at least in these presented examples. Moreover, limit analysis does not involves stiffness matrix and solve linear equations, hence we do not discuss on the rank deficiency here. It is interesting to point out that the collapse multipliers obtained using regular elements ($\alpha_{ir} = 0$) is lower than those of distorted elements (Table IV). This can be explained by the fact that a better (lower) collapse load multiplier may be obtained if elements are adjusted so that its edges match to the slip-lines of the real mechanism [5], but here when distorted meshes are used, elements are aligned randomly, and as a result no improved results were achieved when increasing the level of nodal irregularity.

Next, the efficacy of the proposed method can be demonstrated by comparing the present results with those obtained previously. Note that solutions obtained using CS-FEM1 with regular elements will be employed for comparison due to its advantages mentioned in the previous paragraphs. A convergence analysis is shown in Table V and Figure 11. It can be seen that for all meshes the present solutions are in good agreement with those obtained in [2].

Table IV. Collapse multiplier: distorted meshes with 48×48 elements ($a = 1/2$)

Models	Distortion parameter α_{ir}					
	0	0.2	0.4	0.6	0.8	1
CS-FEM1	1.1504	1.1508	1.1540	1.1554	1.1678	1.1768
FEMRI	1.1504	1.1508	1.1540	fail	fail	fail

Table V. Collapse multiplier: CS-FEM1 with regular meshes

N	$a = 1/3$	$a = 1/2$	$a = 2/3$
6	1.0166	1.2684	1.4746
12	0.9764	1.2035	1.4716
24	0.9513	1.1685	1.4286
48	0.9378	1.1504	1.4065
60	0.9351	1.1467	1.4020
120	0.9296	1.1393	1.3928
160	0.9259	1.1374	1.3837

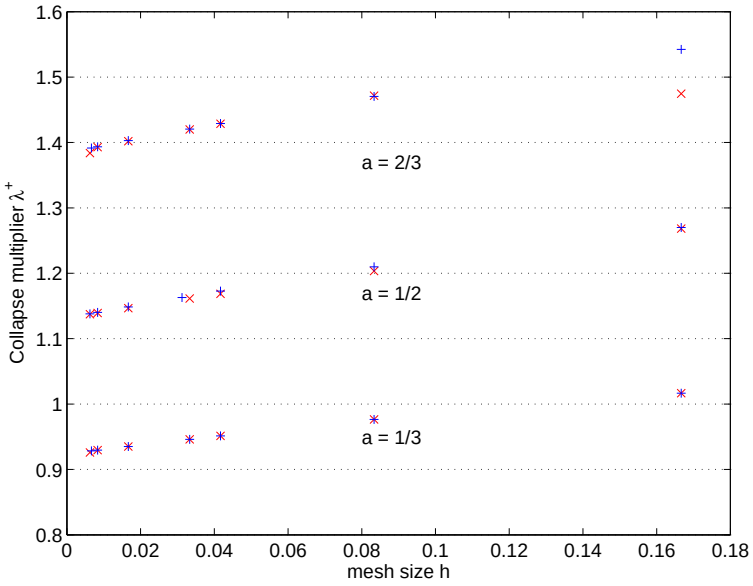

Figure 11. Computed collapse multipliers for different values of a: $\times$ present solutions; $+$ results taken from [2]

Table VI compares solutions computed using the present procedure and $N = 160$ with those in the literature. In general, the present solutions are in good agreement with those obtained previously, particular with results in [2, 7]. However, in [2] they used up to $4 \times 240 \times 240$

linear-linear triangle elements, compared with 160×160 quadrilateral elements used in the present method. Although in [7] only 120×120 elements were used, the corresponding number of degrees of freedom (dof) is up to $4 \times 120 \times 120$ which is significantly larger than that in our procedure ($2 \times 160 \times 160$ dof). Considering previously obtained upper bound solutions, the present method provides lower (more accurate) solutions than in [5] if a regular discretization and the same mesh size are used. The optimization problem corresponding to the 160×160 mesh has 128,642 variables and 77,043 constraints. Very short CPU time (50 seconds) and few iterations (19) were needed to solve this problem. This confirms that the SOCP algorithm can handle efficiently large scale optimization problems.

Table VI. Collapse load multiplier with different values of a and $N = 160$ compared with previously obtained solutions

Approach	Authors	Values of a		
		$a = 1/3$	$a = 1/2$	$a = 2/3$
Kinematic	Ciria et al. [5]			
	- Uniform refinement	–	1.149	–
	- Adaptive refinement	–	1.139	–
	Present method	0.926	1.137	1.384
Mixed formulation	Christiansen and Andersen [2]	0.926	1.136	1.388
	Andersen et al. [7]	0.927	1.137	1.389
Static	Ciria et al. [5]			
	- Uniform refinement	–	1.131	–
	- Adaptive refinement	–	1.132	–
	Krabbenhoft and Damkilde [57]	–	1.132	–
	Tin-Loi and Ngo [6]	0.947‡	1.166‡	1.434‡

‡ where a true lower bound on collapse limit is not guaranteed

The patterns of plastic energy dissipation and collapse mechanisms for different values of a were also shown in Figures 12, 13 and 14. It can be observed that these dissipation patterns are clearly identified in the form of slip lines.

6.3. Prandtl's punch problem

This classical plane strain problem was originally investigated by Prandtl [58], which consists of a semi-infinite rigid-plastic von Mises medium under a punch load, as shown in Figure 15. For a load of $2\tau_0$, the analytical collapse multiplier is $\lambda = 2 + \pi = 5.142$. Since the collapse mechanism is not unique, the punch problem has been solved using continuous [1, 4], semi-continuous [9] or truly discontinuous [59] representations of the velocity field. The present method does not involve discontinuities, similar to the methods used in [1, 4]. The strong discontinuity at the footing edge is a severe challenge to the proposed numerical procedure.

Due to symmetry, only half of the foundation is considered. The rectangular region of $B = 5$ and $H = 2$ was considered sufficiently large to ensure that rigid elements show up along the entire boundary. The punch is represented by a uniform vertical load and appropriate boundary

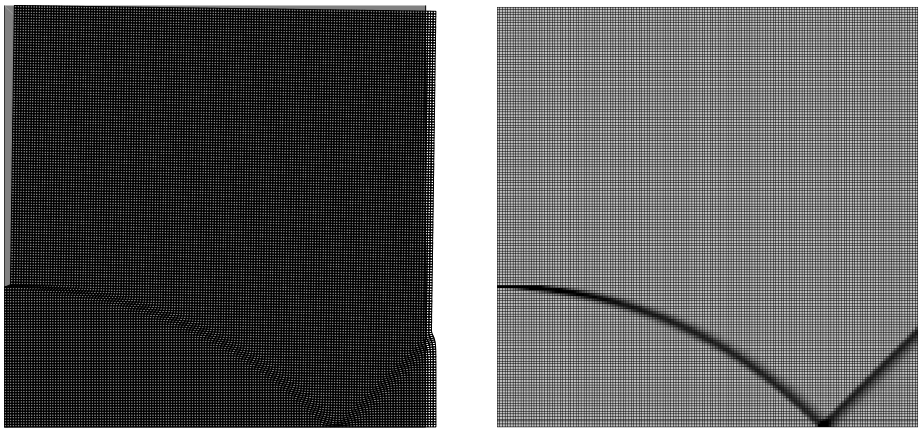

Figure 12. Collapse mechanism (left) and plastic dissipation distribution (right) with $a = 1/3$

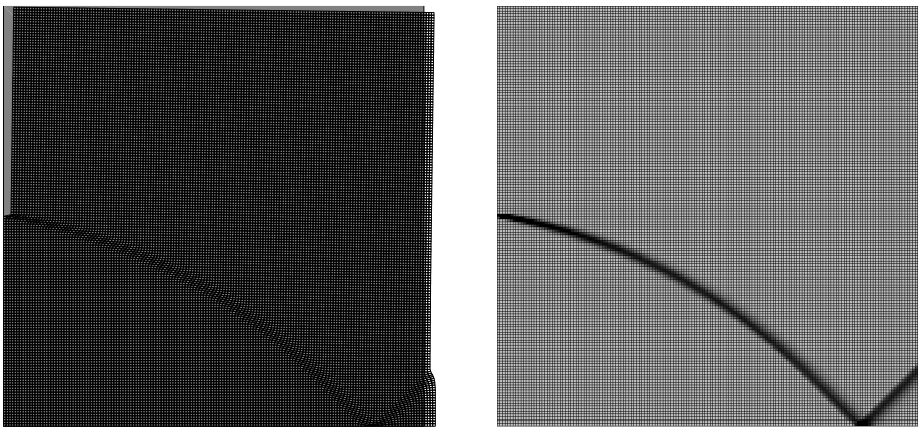

Figure 13. Collapse mechanism (left) and plastic dissipation distribution (right) with $a = 1/2$

conditions were applied, as shown in Figure 16.

The problem has been solved using CS-FEM1. Collapse multipliers and associated errors for various meshes are shown in Table VII. It can be observed that the solutions obtained using the present method show a very good accuracy when compared with the analytical solution. For all meshes, the relative errors to the exact solution are smaller than 1%, particularly a mesh of just 40 four-node quadrilateral elements can provide an extremely satisfactory solution with only 0.8% error. Furthermore, all the solutions obtained are again above the exact value. This indicates that the presented procedure is capable of producing an upper bound on the actual collapse load multiplier.

Table VIII compares solutions obtained using the present method with upper and lower bound solutions that have previously been reported in the literature. The present results are proved to be competitive with those obtained by other methods. Considering previously

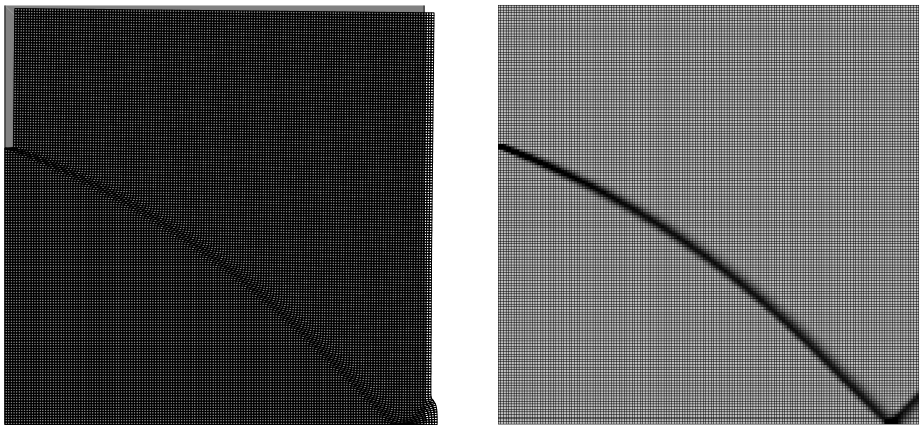

Figure 14. Collapse mechanism (left) and plastic dissipation distribution (right) with $a = 2/3$

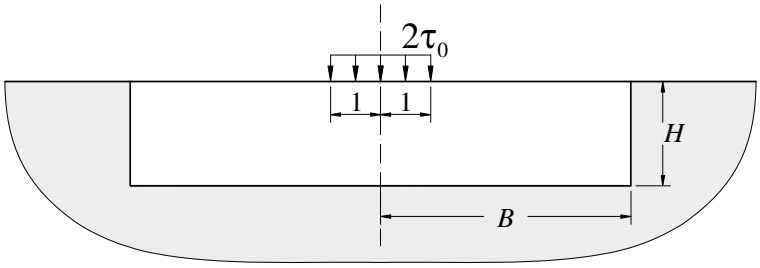

Figure 15. Prandtl's punch: geometry and loading

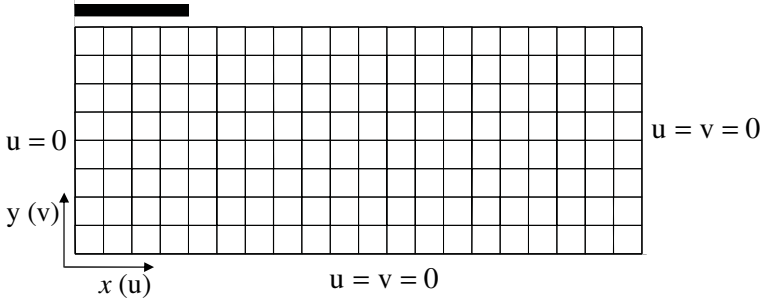

Figure 16. Finite element mesh and displacement boundary conditions

obtained upper bound solutions, the present method provides lower (more accurate) upper bound solutions than in [4, 9, 42]. While in [4] a mesh of 4784 three-node elements was used to achieve a solution of 5.264, Sloan & Kleeman [9] can provide a lower solution with 1.32% error using only 384 constant strain elements combining with 556 velocity discontinuities. It turns out that using discontinuity in the displacement field can help to increase the accurate of the

Table VII. The punch problem: collapse multiplier

Models	Number of elements					
	40	160	640	2560	5760	10240
CS-FEM1	5.1809	5.1550	5.1474	5.1441	5.1432	5.1427
Error (%)	0.76	0.25	0.11	0.04	0.02	0.01

solution. However, it is not the only possible choice, as shown here, since the use of a strain smoothing technique is capable of producing an accurate solution. In addition, the solution of the finest mesh used here is also lower than the best upper bound in [42] using a mesh of up to 18719 six-node triangle elements, which was generated with reduced element size close to the footing.

Table VIII. Collapse load multiplier compared with previously obtained solutions

Approach	Authors	Collapse multiplier	Error (%)
Kinematic	Vicente da Silva and Antao [4]	5.264	+2.37
	Sloan & Kleeman [9]	5.210	+1.32
	Makrodimopoulos & Martin [42]	5.148	+0.12
	Present method	5.143	+0.02
Mixed formulation	Capsoni & Corradi [1]	5.240	+1.90
Analytical solution	Prandtl [58]	5.142	–
Static	Makrodimopoulos & Martin [60]	5.141	-0.02
	Tin-Loi and Ngo [6]	5.173‡	+0.60

‡ where a true lower bound on collapse limit is not guaranteed

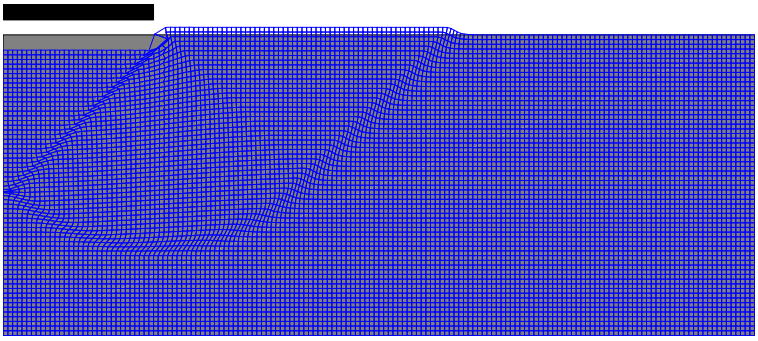

Figure 17. The punch problem: collapse mechanism

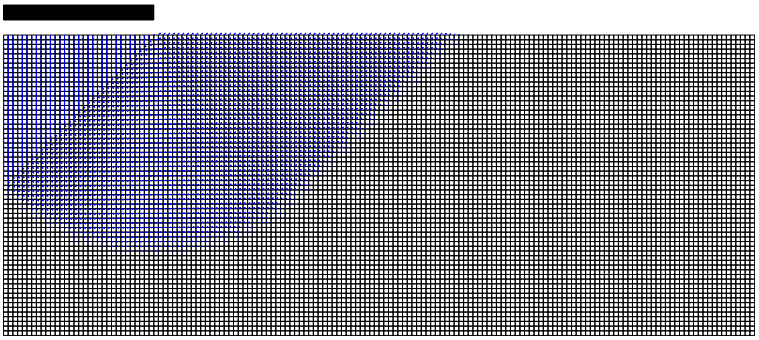

Figure 18. The punch problem: velocity field

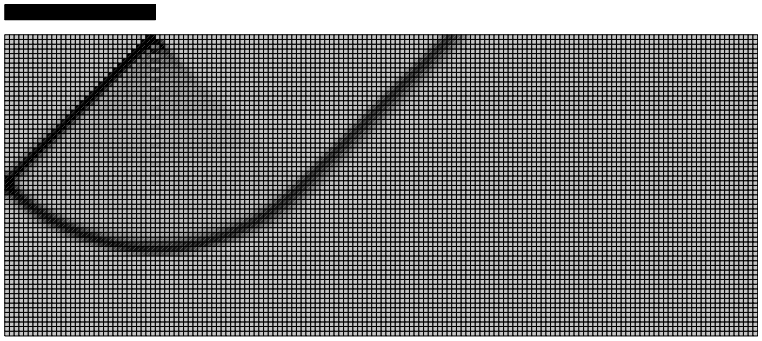

Figure 19. The punch problem: plastic dissipation distribution

Collapse mechanisms, the velocity field and the patterns of plastic energy dissipation for the mesh of 10240 elements are illustrated in Figures 17, 18 and 19, respectively. The mechanism is identical to the one given by Prandtl [58]. Note that in the present work the mesh is refined uniformly without taking advance of *a priori* knowledge of the collapse mechanism. This results in a unnecessary refinement in the rigid regions. This motivates immediately the need of an adaptive scheme to recognize and refine automatically the plastic regions. The pattern of slip lines is again clearly identified.

7. CONCLUSIONS

A novel numerical procedure for kinematic limit analysis of plane problems has been proposed. Together with [15], this paper demonstrates that a numerical limit analysis procedure using a strain smoothing technique is capable of providing accurate solutions using a relatively small number of elements (nodes). It was also shown that most properties of CS-FEM found in elastic analysis, for instance superconvergent behavior, working well for extremely distorted elements and locking free behaviour (using one cell version), are retained here in plastic limit analysis. Moreover, the proposed method using CS-FEM in combination with second-

order cone programming can solve efficiently real-world problems in engineering practice. Although the procedure cannot be guaranteed to produce strict upper bound solutions, for the plane stress and plane strain problems, investigated solutions were in practice always higher than known exact solutions, and lower than existing upper bound numerical solutions in the literature. It is also worth noting that the method is able to capture slip line patterns arising from localized plastic deformations for problems of arbitrary geometry.

Finally, although only plane problems are considered here, the numerical procedure can be extended to tackle more complex structural configurations such as shells, 3D problems. It would also be interesting to combine the proposed method with an adaptive refinement to speed-up the computational process.

REFERENCES

1. A. Capsoni and L. Corradi. A finite element formulation of the rigid-plastic limit analysis problem. *International Journal for Numerical Methods in Engineering*, 40:2063–2086, 1997.
2. E. Christiansen and K. D. Andersen. Computation of collapse states with von Mises type yield condition. *International Journal for Numerical Methods in Engineering*, 46:1185–1202, 1999.
3. K. Krabbenhoft and L. Damkilde. A general nonlinear optimization algorithm for lower bound limit analysis. *International Journal for Numerical Methods in Engineering*, 56:165–184, 2003.
4. M. Vicente da Silva and A. N. Antao. A non-linear programming method approach for upper bound limit analysis. *International Journal for Numerical Methods in Engineering*, 72:1192–1218, 2007.
5. H. Ciria, J. Peraire, and J. Bonet. Mesh adaptive computation of upper and lower bounds in limit analysis. *International Journal for Numerical Methods in Engineering*, 75:899–944, 2008.
6. F. Tin-Loi and N. S. Ngo. Performance of the p-version finite element method for limit analysis. *International Journal of Mechanical Sciences*, 45:1149–1166, 2003.
7. K. D. Andersen, E. Christiansen, and M. L. Overton. Computing limit loads by minimizing a sum of norms. *SIAM Journal on Scientific Computing*, 19:1046–1062, 1998.
8. A. Bottero, R. Negre, J. Pastor, and S. Turgeman. Finite element method and limit analysis theory for soil mechanics problems. *Computer Methods in Applied Mechanics and Engineering*, 22:131–149, 1980.
9. S. W. Sloan and P. W. Kleeman. Upper bound limit analysis using discontinuous velocity fields. *Computer Methods in Applied Mechanics and Engineering*, 127:293–314, 1995.
10. A. V. Lyamin and S. W. Sloan. Upper bound limit analysis using linear finite elements and nonlinear programming. *International Journal for Numerical and Analytical Methods in Geomechanics*, 26:181–216, 2002.
11. J. S. Chen, C. T. Wux, S. Yoon, and Y. You. A stabilized conforming nodal integration for Galerkin mesh-free methods. *International Journal for Numerical Methods in Engineering*, 50:435–466, 2001.
12. K. Y. Sze, J. S. Chen, N. Sheng, and X. H. Liu. Stabilized conforming nodal integration: exactness and variational justification. *Finite Elements in Analysis and Design*, 41:147–171, 2004.
13. D. Wang and J. S. Chen. Locking-free stabilized conforming nodal integration for meshfree Mindlin-Reissner plate formulation. *Computer Methods in Applied Mechanics and Engineering*, 193:1065–1083, 2004.
14. J. S. Chen, S. Yoon, and C. T. Wu. Non-linear version of stabilized conforming nodal integration for Galerkin mesh-free methods. *International Journal for Numerical Methods in Engineering*, 52:2587–2615, 2002.
15. C. V. Le, M. Gilbert, and H. Askes. Limit analysis of plates using the EFG method and second-order cone programming. *International Journal for Numerical Methods in Engineering*, 78:1532–1552, 2009.
16. C. V. Le, H. Askes, and M. Gilbert. Adaptive Element-Free Galerkin method applied to the limit analysis of plates. *Computer Methods in Applied Mechanics and Engineering*, 2009, submitted.
17. C. V. Le, M. Gilbert, and H. Askes. Limit analysis of plates and slabs using a meshless equilibrium formulation. *International Journal for Numerical Methods in Engineering*, 2009, submitted.
18. G. R. Liu, K. Y. Dai, and T. T. Nguyen. A smoothed finite element method for mechanics problems. *Computational Mechanics*, 39:859–877, 2007.
19. G. R. Liu, T. T. Nguyen, K. Y. Dai, and K. Y. Lam. Theoretical aspects of the smoothed finite element method (SFEM). *International Journal for Numerical Methods in Engineering*, 71:902–930, 2007.
20. H. Nguyen-Xuan, S. Bordas, and H. Nguyen-Dang. Smooth finite element methods: Convergence, accuracy and properties. *International Journal for Numerical Methods in Engineering*, 78:175–208, 2008.

21. T.T. Nguyen, G.R. Liu, K.Y. Dai, and K.Y. Lam. Selective smoothed finite element method. *Tsinghua Science and Technology*, 12:497 – 508, 2007.
22. K. Y. Dai and G. R. Liu. Free and forced vibration analysis using the smoothed finite element method (SFEM). *Journal of Sound and Vibration*, 301:803–820, 2007.
23. H. Nguyen-Xuan, T. Rabczuk, S. Bordas, and J. F. Debongnie. A smoothed finite element method for plate analysis. *Computer Methods in Applied Mechanics and Engineering*, 197:1184–1203, 2008.
24. N. Nguyen-Thanh, T. Rabczuk, H. Nguyen-Xuan, and S. Bordas. A smoothed finite element method for shell analysis. *Computer Methods in Applied Mechanics and Engineering*, 198:165–177, 2008.
25. H. Nguyen-Xuan, S. Bordas, and H. Nguyen-Dang. Addressing volumetric locking and instabilities by selective integration in smoothed finite elements. *Communications in Numerical Methods in Engineering*, 25:19–34, 2009.
26. H. Nguyen-Xuan and T. Nguyen-Thoi. A stabilized smoothed finite element method for free vibration analysis of Mindlin-Reissner plates. *Communications in Numerical Methods in Engineering*, 25:882–906, 2009.
27. S.P.A. Bordas, T. Rabczuk, H. Nguyen-Xuan, V. P. Nguyen, S. Natarajan, T. Bog, Q.M. Do, and H. Nguyen-Vinh. Strain smoothing in FEM and XFEM. *Computers and Structures*, *in press, doi:10.1016/j.compstruc.2008.07.006*, 2009.
28. G.R. Liu, T. Nguyen-Thoi, H. Nguyen-Xuan, and K.Y. Lam. A node-based smoothed finite element method (NS-FEM) for upper bound solutions to solid mechanics problems. *Computers and Structures*, 87:14–26, 2009.
29. G.R. Liu, T. Nguyen-Thoi, and K.Y. Lam. An edge-based smoothed finite element method (ES-FEM) for static, free and forced vibration analyses of solids. *Journal of Sound and Vibration*, 320:11001130, 2009.
30. H. Nguyen-Xuan, GR Liu, T.Nguyen-Thoi, and C. Nguyen Tran. An edge-based smoothed finite element method (ES-FEM) for analysis of two-dimensional piezoelectric structures. *Journal of Smart Material and Structures*, 12:065015 (12pp), 2009.
31. T. Nguyen-Thoi, G.R. Liu, K.Y. Lam, and G.Y. Zhang. A Face-based Smoothed Finite Element Method (FS-FEM) for 3D linear and nonlinear solid mechanics problems using 4-node tetrahedral elements. *International Journal for Numerical Methods in Engineering*, 78:324–353, 2009.
32. E. Anderheggen and H. Knopfel. Finite element limit analysis using linear programming. *International Journal of Solids and Structures*, 8:1413–1431, 1972.
33. H. Huh and W. H. Yang. A general algorithm for limit solutions of plane stress problems. *Journal of Solids and Structures*, 28:727–738, 1991.
34. G. L. Jiang. Non linear finite element formulation of kinematic limit analysis. *International Journal for Numerical Methods in Engineering*, 38:2775–2807, 1995.
35. H. Huh, C. H. Lee, and W. H. Yang. A general algorithm for plastic flow simulation by finite element limit analysis. *Journal of Solids and Structures*, 36:1193–1207, 1999.
36. A. Chaaba, L. Bousshine, and G. De Saxce. Kinematic limit analysis modelling by a regularization approach and finite element method. *International Journal for Numerical Methods in Engineering*, 57:1899–1922, 2003.
37. N. Zouain, J. Herskovits, L. A. Borges, and R. A. Feijoo. An iterative algorithm for limit analysis with nonlinear yield functions. *International Journal of Solids and Structures*, 30:1397–1417, 1993.
38. Y. H. Liu, Z. Z. Zen, and B. Y. Xu. A numerical method for plastic limit analysis of 3-D structures. *International Journal of Solids Structures*, 32:1645–1658, 1995.
39. K. D. Andersen, E. Christiansen, and M. L. Overton. An efficient primal-dual interior-point method for minimizing a sum of Euclidean norms. *SIAM Journal on Scientific Computing*, 22:243–262, 2001.
40. E. D. Andersen, C. Roos, and T. Terlaky. On implementing a primal-dual interior-point method for conic quadratic programming. *Mathematical Programming*, 95:249–277, 2003.
41. Mosek. *The MOSEK optimization toolbox for MATLAB manual. http://www.mosek.com.* Mosek ApS, version 5.0 edition, 2009.
42. A. Makrodimopoulos and C. M. Martin. Upper bound limit analysis using simplex strain elements and second-order cone programming. *International Journal for Numerical and Analytical Methods in Geomechanics*, 31:835–865, 2006.
43. J. J. Munoz, J. Bonet, A. Huerta, and J. Peraire. Upper and lower bounds in limit analysis: Adaptive meshing strategies and discontinuous loading. *International Journal for Numerical Methods in Engineering*, 77:471–501, 2009.
44. C. V. Le, H. Nguyen-Xuan, and H. Nguyen-Dang. Upper and lower bound limit analysis of plates using FEM and second-order cone programming. *Computers and Structures*, 2009, accepted.
45. J. W. Yoo, B. Moran, and J. S Chen. Stabilized conforming nodal integration in the natural-element method. *International Journal for Numerical Methods in Engineering*, 60:861–890, 2004.
46. J. S. Chen, C. T Wu, and T. Belytschko. Regularization of material instabilities by meshfree approximations with intrinsic length scales. *International Journal for Numerical Methods in Engineering*,

47:1303–1322, 2000.
47. T. Belytschko. Plane stress shakedown analysis by finite elements. *International Journal of Mechanical Sciences*, 14:619–625, 1972.
48. H. Nguyen-Dang and L. Palgen. Shakedown analysis by displacement method and equilibrium finite elements. page L3/3. Proceedings of SMIRT-5, Berlin, 1979.
49. J. Gross-Weege. On the numerical assessment of the safety factor of elasto-plastic structures under variable loading. *International Journal of Mechanical Sciences*, 39:417–433, 1997.
50. Y. Liu, X. Zhang, and Z. Cen. Numerical determination of limit loads of three-dimensional structures using boundary element method. *European Journal of Mechanics A/Solids*, 23:127–138, 2004.
51. S. Chen, Y. Liu, and Z. Cen. Lower-bound limit analysis by using the EFG method and non-linear programming. *International Journal for Numerical Methods in Engineering*, 74:391–415, 2008.
52. F.A. Gaydon and A. W. McCrum. A theoretical investigation of the yield-point loading of a square plate with a central circular hole. *Journal of Mechanics and Physics of Solids*, 2:156–169, 1954.
53. N. Zouain, L. Borges, and J. L. Silveira. An algorithm for shakedown analysis with nonlinear yield functions. *Computer Methods in Applied Mechanics and Engineering*, 191:2463–2481, 2002.
54. J. C. Nagtegaal, D. M. Parks, and J. C. Rice. On numerically accurate finite element solutions in the fully plastic range. *Computer Methods in Applied Mechanics and Engineering*, 4:153–177, 1974.
55. K. D. Andersen and E. Christiansen. Limit analysis with the dual affine scaling algorithm. *Journal of Computational and Applied Mathematics*, 59:233–243, 1995.
56. E. Christiansen and O. S. Pedersen. Automatic mesh refinement in limit analysis. *International Journal for Numerical Methods in Engineering*, 50:1331–1346, 2001.
57. K. Krabbenhoft and L. Damkilde. A general nonlinear optimization algorithm for lower bound limit analysis. *International Journal for Numerical Methods in Engineering*, 56:165–184, 2003.
58. L. Prandtl. Ueber die haerte plastischer koerper. *Nachrichtex der Akademie der Wissenschaften in Gottingen. II. Mathematisch-Physikalische Klasse II*, 12:74–85, 1920.
59. C. C. Smith and M. Gilbert. Application of Discontinuity Layout Optimization to Plane Plasticity Problems. *Proc. R. Soc. A.*, 463:2461–2484, 2007.
60. A. Makrodimopoulos and C. M. Martin. Lower bound limit analysis of cohesive-frictional materials using second-order cone programming. *International Journal for Numerical Methods in Engineering*, 66:604–634, 2006.